UNIVERSITAT POLITÈCNICA DE CATALUNYA
BARCELONATECH
Escola d'Enginyeria de Telecomunicació
i Aeroespacial de Castelldefels

Master Thesis

TITLE: Design and implementation of an electronic system for a microgravity experiment

DEGREE: Master's degree in Aerospace Science and Technology

AUTHOR: Ioana El Kraye Ziade

DIRECTED BY: Ricard González Cinca

DATE: September 4, 2022

Title : Design and implementation of an electronic system for a microgravity experiment
Author: Ioana El Kraye Ziade

Directed by: Ricard González Cinca

Date: September 4, 2022

Overview

Space missions are increasing in complexity and duration, so do both power and heat dissipation demands. Electronic devices are miniaturized to fit into compact spaces, whilst the processing speed and memory capacity is increasing constantly, leading to higher power consumption. As most of the electric power consumed transforms into heat, electronic components are more prone to failure due to overheating. The absence of buoyancy in microgravity results in an increase in the surface temperature of electric devices. As the performance and the failure process of electronics depend on their operational temperature range, effective cooling techniques are becoming more important.

The ability to reduce the size, weight, power consumption and cost of cooling technologies will have a major impact on thermal management systems. A simple technique for cooling electronics based on acoustic actuation on multiphase flows is proposed.

The focus of this thesis is to design and develop a complete electronic system consisting of a heating subsystem, an acoustic wave subsystem, and an instrumentation subsystem for an experiment in microgravity. The aim of this work is to ensure the correct performance of all these subsystems in order to demonstrate that convection can be achieved using acoustic waves in microgravity conditions.

Escriure aqui
la dedicatòria

CONTENTS

LIST OF FIGURES

LIST OF TABLES

INTRODUCTION

Space missions are increasing in complexity and duration, and so do both power and heat dissipation demands. Electronic devices are miniaturized to fit into compact spaces, whilst the processing speed and memory capacity is increasing constantly, leading to higher power consumption. As most of the electric power consumed disperses into heat, electronic components are more prone to failure due to overheating. Black's median time to failure equation demonstrates that a moderate rise in the operational temperature could accelerate exponentially the failure rate of the component [1]. According to Pedram and Nazarian, a large proportion of electronic circuit failures are caused by high temperatures, sudden temperature variations, and the presence of hot spots [2].

As electronic components are becoming smaller and more compact, the space to place heat sinks, liquid loops and fans is significantly reduced. According to Behnia et al., miniaturized devices present an increase in the complexity of the heat transfer path from the heat dissipating components to the outer surface of the system [3].

In all electrical systems there are specific thermal management requirements from high heat flux, low pressure drop and high heat transfer coefficient to weight, reliability and safety. Conforming to Tustain, the requirements to derate temperature limits of the device in accordance to product assurance standards, such as the European Cooperation for Space Standardization (ECSS), adds difficulties since the thermal margin within the design is reduced [4].

Heat transfer from natural convection is affected by the magnitude of the gravity level. On Earth, where the effects of gravity are dominant, heat transfer from electric devices to the surrounding medium is achieved through natural convection. The absence of buoyancy in microgravity results in an increase in the surface temperature of electric devices. With the increase of heat dissipated by on-board electronics and the absence of natural convection, thermal issues are likely to become more prevalent for future space missions [5].

In summary, microgravity poses great challenges on cooling technologies since both the performance and the failure process of electronics depend on their operational temperature range. With the increasing heat dissipation demands and thermal management challenges in low gravity conditions, innovative techniques are required to enhance the heat transfer rate. The ability to reduce the size, weight, power consumption and cost of cooling technologies will have a major impact on thermal management systems.

The proposed approach is inspired from previous studies carried out at the UPC Space Exploration Lab. It uses acoustic waves to increase the heat transfer from a heat source and ambient air. With the absence of natural convection, higher heat transfer rates can be obtained by exerting an external forced flow. Acoustic wave can generate these flows without using mechanical fans or liquid loops.

This experiment has been selected for the Drop Your Thesis! programme which offers students the possibility to perform scientific research in a drop tower. Therefore, the ex-

perimental setup is designed to test acoustic waves cooling technique at the ZARM drop tower in November 2022. This educational program helps students gain experience in scientific experiments design and project organization while working in a diverse team. A board consisting of ZARM engineers and ESA personnel provides technical support to the teams throughout the development of the project.

During the campaign, the experiment will be integrated into a capsule that is launched from the bottom of the tower up to 120 meters in near vacuum. This environment allows low and accurate microgravity levels of $10^{-6}g$. By using the catapult mode, the microgravity period can be extended to 9.3 seconds. Multiple experiment runs are possible during the campaign. In our case, five launches with different experimental procedures will be realized.

This thesis covers the electronics section of the experiment. The first chapter includes the state of the art. The second chapter presents the requirements for the hardware section of the experiment followed by a description of the experimental setup. Chapter four covers the circuit design and analysis. Finally, the designed printed circuit boards (PCBs) for the experiment are shown in chapter 5.

CHAPTER 1. STATE OF THE ART

1.1. Current Cooling Techniques

Most of the current cooling techniques are based on liquid cooling and phase change principles. Heat is transported away from the heated surfaces either directly, when the coolant and the electric component are in direct contact, or indirectly, when the coolant is pumped through a heat exchanger. Different direct cooling techniques are described in the next paragraph followed by indirect cooling techniques.

Natural convection of air, with no external mechanism, is characterized by a change of the fluid density with temperature. This method is very common, however, heat dissipation is limited which makes it unsuitable for high power devices. By adding a fan and a heat sink, forced air convection can be created. Heat dissipation through a heat sink depends on the thermal conductivity, thermal resistance and the effective surface area of the sink. Acikalin et al. in [6] studied piezoelectric fans as an active cooling technique for smaller devices where rotary fans are not applicable. The setup consisted of a 0.19 mm thick piezoelectric transducer that was attached to short blades of 2.8 cm with oscillation frequencies of 110 Hz. The fans were placed near power electronics of a commercial laptop where a temperature drop of 6 °C was reported. Jet impingement is another direct cooling technique that creates an airflow near the heated surface, however, external mechanisms such as compressors are required to reach heat fluxes of $60\ W/cm^2$ [7]. Lin et al. in [8] investigated the effects of thermoacoustics, thermally induced acoustic waves, on heat transfer in normal and low gravity conditions. The computational and experimental results in a cylindrical resonator demonstrated that convection induced by acoustic streaming has a marked effect on heat transfer [8].

Micro-channels and pin fins are being added on the surface of IC chips for increased heat transfer. However, there are challenges from transforming micro-scale cooling systems to a macro-scale technology. The highest macro-scale heat transfer values can be reached by using phase change principles [7]. In this case, the evaporated liquid transports large quantities of heat to the condenser where the vapor turns back into liquid. Thus, the heat transfer depends severely on the geometry and orientation of the heat pipe which reduces the design flexibility. Passive cooling methods, PCMs, are relatively a new cooling technology that promises temperature stability by absorbing large quantities of heat [9]. Nevertheless, the design of these cooling techniques is generally more complex and often more complicated when considering gravitational and frictional effects.

1.2. Cooling Techniques in Space

This paragraph introduces different equipment on board of the ISS along their thermal control system based on [10]. The purpose of the Photovoltaic Thermal Control System (PVTCS) is to eliminate the excess heat from the Electrical Power System (EPS) components in the Integrated Equipment Assembly (IEA). PVTCS are able to dissipate $6000\ W$ of heat per orbit while its pump flows consume around $500\ W$ during normal operations.

Ammonia loop supplies coolant to cold plates to remove heat from Direct Current-to-Direct Current Units (DDCUs) and Main Bus Switch Units (MBSUs). For the DDCUs, the plate can remove $495\ W$ at $36\ Kg/hr$, whereas for the MBSUs the plate can remove $694\ W$ at $57\ Kg/hr$.

For the World Space Observatory UV Spectrographs (WUVS), instrument used in a mission led by Roskosmos, the Camera Electronics Box (CEB) that drives the instrument is cooled by a thermal plate to remove the hot spots within the electronics that are caused by high power dissipating components on the printed circuit boards. The total power dissipated by the CEB is $14.7\ W$ [4]. Moreover, the PCB components inside the CEB have defined temperature limits which are then derated by $40\ ^oC$ according to ECSS standards [4].

1.3. Heat transfer and acoustics in air

There have been some experimental studies on the interaction between heat transfer and acoustics in normal gravity conditions. The heat transfer coefficient increased significantly when an acoustic wave was applied [11]. The results of convective heat transfer rates from an isolated sphere in the presence of standing acoustic waves showed a temperature difference of $42.8\ K$ [12]. The use of ultrasound resulted in an increase of the hear transfer coefficient by 45% to over 200%, but it was found that the heat transfer coefficient highly depends on the shape of the examined samples [13]. An increase of the heat transfer coefficient from $10.92\ W/m^2K$ to $13.04\ W/m^2K$ when an acoustic wave of $200\ Hz$ was applied [14].

1.4. Acoustics in microgravity

Acoustic actuation in microgravity increased the heat flux from a heater to a liquid by 8.4% compared to scenarios without actuation thanks to an acoustic-induced convection [15]. In summary, acoustic actuation is an efficient approach for heat transfer enhancement in multiphase flows in terrestrial gravity.

Kumar et al. proved that by using ultrasonic standing wave, acoustic fields have great potential in the field of heat transfer [16]. The method studied showed that the acoustic fields, without gravity, can enhance the heat transfer by 11 times compared to the heat transfer due to only conduction [16].

CHAPTER 2. EXPERIMENTAL SET-UP

The experimental setup for the study of the acoustic technique consists of a test cell and subsystems for heat generation, acoustic wave generation and data acquisition. Figure 2.1 illustrates the elements that are placed inside the test cell.

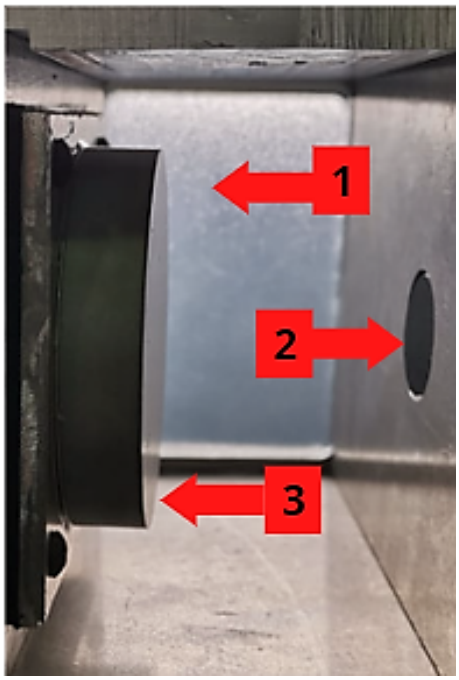

Figure 2.1: Test cell components: (1) granulated background; (2) ceramic heater; (3) piezoelectric transducer.

2.0.1. Heat generation subsystem

The heat generation subsystem consists of a ceramic heater and heat control PCB designed to control the power supplied to the heater.

A Nichrome wire was initially used for the heater design. Different shapes were tested, such as helical coil, straight wire and serpentine. None of the three designs was selected due to these main reasons: The presence of heat spots near the cable connections obstructing the heat flux produced by the heater, and the heater's shape is deformed after several testings.

Therefore, commercial ceramic heater was selected to ensure that the surface is heated evenly with no hot spots, as they can disturb the data analysis.

2.0.2. Acoustic wave generation subsystem

The acoustic wave generation subsystem consists of a ceramic piezoelectric transducer (PZT), a function generator and an amplifier.

The distance between the PZT and the heater is determined by the frequency of the acoustic actuation. The resonance frequency of the PZT provides a wave with the highest amplitude and, hence, is likely to generate the strongest effect on the gas flow. The role of the function generator is to produce the desired sinusoidal signal, with a specific frequency and amplitude, and send it to the amplifier. When the signal reaches the piezoelectric transducer, the acoustic wave is generated due to the piezoelectric effect.

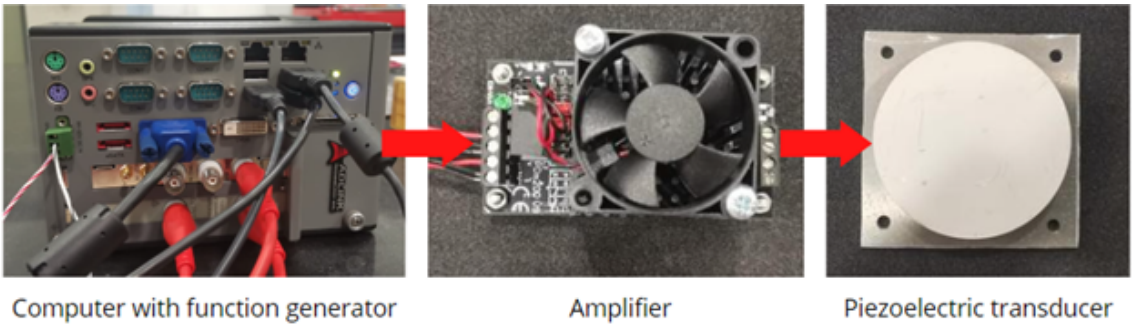

Figure 2.2: Acoustic wave generation subsytem hardware.

2.0.3. Data acquisition subsystem

The data acquisition function is to measure and visualise the heat transfer created by the propagation of the acoustic wave.

Thermocouples are used in the setup to detect variations in temperature inside the heater and in its surroundings. Those will be strategically placed on the surroundings of the heater to perceive any change in the shape of the heat flux due to the acoustic field applied.

A thermal camera is used to measure the temperature of the heater and to visualize the temperature distribution on the heater surface. In addition to that, high speed camera recordings are used to depict the changes in density caused by the application of the acoustic wave by applying Background Oriented Schlieren technique (BOS). This requires that the test cell has two windows: a transparent one to enable the recording, and a second one with a background pattern. A LED matrix PCB will be placed behind the patterned window to provide adequate lighting conditions for the recording.

CHAPTER 3. REQUIREMENTS

The following sections state the experiment requirements related to electronics and their different status regarding verification, to that end some abbreviations will be used. T for verification by testing, A for verification by analysis or similarity, R for review of design and I for verification by inspection.

3.1. Performance Requirements

Performance requirements are quantifiable and defines the range over which the function is performed, the expected throughput, and the system's capabilities.

ID	Requirement	Verification
P.1.1	The piezoelectric transducer shall be powered with 30W.	R,T
P.1.2	The voltage supplied to the piezoelectric transducer shall be between ±150V.	R
P.1.3	The heater shall be provided with power up to 50W.	R,T
P.1.4	The temperature measurement near the heater shall be made with a range of accuracy of ±1 ℃	R,T
P.1.5	The temperature measurement near the heater shall be made with a precision of ±1 ℃.	R,T
P.1.6	The temperature measurement near the heater shall be made within the range 0 ℃ to 250 ℃.	R,T
P.1.7	The ambient temperature inside the test cell shall be measured between 0 and 250 ℃.	R,T
P.1.8	The temperature measurements shall filter the noise lower than 11Hz.	R,T
P.1.9	The temperature of the heater shall be measured up to 250 ℃.	R,T
P.1.10	The temperature measurement of the heater shall be made with a range of accuracy of ±1 ℃.	R,T
P.1.11	The temperature measurement of the heater shall be made with a precision of ±1 ℃.	R,T

Table 3.1: Performance Requirements list and verification

3.2. Design Requirements

The design requirements define the aspects that are imposed by the platform and program. The following design requirements is from ZARM's drop tower experiment support [17].

ID	Requirement	Verification
D.1.1	The total power consumption of the experiment should be less than 110W	R,T

Table 3.2: Design Requirements list and verification

3.3. Interface Requirements

Interface requirements are derived from the platform's requirements, in this case [17]. These requirements include some design and safety aspects.

ID	Requirement	Verification
I.1.1	The experiment shall be connected to the battery pack via the Power Distribution Unit	R
I.1.2	The hardware shall operate with a voltage between 22V to 30V	R
I.1.3	The hardware maximum current per channel/pair shall be less than 15A	R
I.1.4	The hardware electrical strength shall be less than 38V DC	R.
I.1.5	All consumers shall be grounded to one identical point on each platform.	R

Table 3.3: Interface Requirements list and verification

3.4. Operational Requirements

These requirements include operating needs and describe how the experiment works.

ID	Requirement	Verification
O.1.1	The acoustic wave generation subsystem shall be activated remotely before the launch.	R,T
O.1.2	The acoustic wave generation subsystem shall be controlled autonomously during the launch.	R.
O.1.3	The heat generation subsystem shall be activated remotely before the launch.	R,T
O.1.4	The heat generation subsystem shall be controlled autonomously during the launch.	R,T
O.1.5	The control panel shall be able to modify the heater voltage input during and after the drop.	R,T

Table 3.4: Operational Requirements list and verification

CHAPTER 4. ELECTRONICS

The power distribution and communication block diagram of the experimental set-up is represented in Figure 4.1. The blocks in green represent the Printed Circuit Boards (PCBs) designed and manufactured for the experiment. Different colours represent the different role of each arrow: red colour is for voltage supply, yellow for data transmission, green for trigger signals, and blue for USB serial connection. The power distribution unit (PDU) of ZARM is directly connected to the DC/DC regulators used in the experiment. The devices used for our experiment require different voltage inputs and the batteries provided by ZARM do not regulate the voltage, therefore, DC/DC regulators are used to supply the devices with the required voltage.

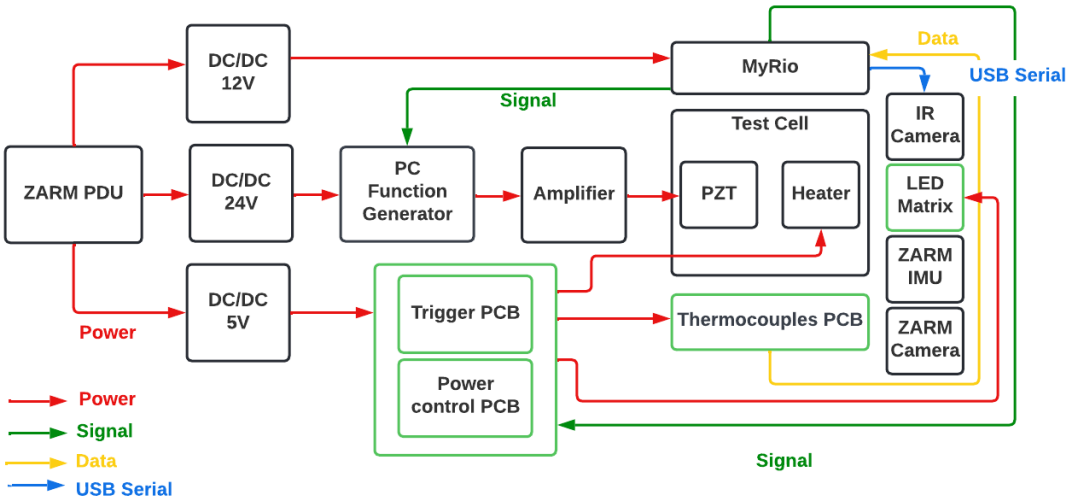

Figure 4.1: General Electrical system diagram.

4.1. DC/DC regulators

A DC/DC regulator is power converter that converts a source of direct current (DC) from one voltage level to another.

As shown in the general electrical system block diagram, the electrical devices and PCBs need different voltages. The overall charging voltage of each battery pack has an overall charging voltage of $27.6V$. During the discharging, the actual output voltage will fluctuate and the PDU may allow tolerance from 22.6 to $30V$. Hence, the DC/DC converters selected should have a wide input range.

The $12V$ DC/DC regulator powers the LED matrix and MyRio. The $24V$ DC/DC regulator powers the PC that includes the function generator. The heater control PCB output is connected to the $24V$ and $12V$ DC/DC regulators to supply the heater with higher power. Finally, the $5V$ DC/DC regulator powers the thermocouples PCB and the relays in the power control and triggers PCB.

The pin connections are identical for both $12V$ and $24V$ DC/DC regulators, Figure.4.2 from the device data sheet [18], and they both have wide voltage input ranges from 9 to $36V$. These two models are designed with a heat sink. This feature is important because it allows to manage the heat properly so the converter maintains operation within the recommended temperature limits.

Pin 1	+Vin
Pin 3	-Vin
Pin 6	+Vout
Pin 7	-Vout

Figure 4.2: 12V DC/DC converter with pins connection.

Regarding the $5V$ DC/DC regulator, TRACO POWER TEN 30-2431WIN model is used. It also has a wide input voltage range of 9V to 36V. The pin connections are indicated in Figure.4.3 obtained from the device data sheet [19].

Pin 1	+Vin
Pin 2	-Vin
Pin 6	-Vout
Pin 7	+Vout

Figure 4.3: 5V DC/DC converter with pins connection.

4.2. Internal Triggers

Internal triggers are used with the scope of activating certain parts of the experiment automatically before and during the drop by receiving a signal from MyRIO. Based on the experimental procedure, the trigger will activate a certain circuit either by using time delay or gravity level as reference. For instance, some electrical devices are activated before the launch to be sure they are operating as intended. For the parameters that are going to be modified during the drop, the IMU measurements from ZARM are used to ensure that the changes occur during the microgravity phase.

The segments that are activated after a time delay are the LED matrix, the thermocouples and the IR camera. The segments that are activated based on microgravity level are the heater power control PCB and the piezoelectric transducer. In addition, all segments should be able to activate and stop using a trigger that is independent from time and microgravity, to ensure that we can start specific circuits for testing or force to stop the segment in case of failure.

4.2.1. Trigger circuit sequence

NPN common emitter relay circuit design is chosen for internal triggers circuit design. This circuit configuration is selected because using the relays alone to activate the targeted circuit requires an amount of current and at least $5V$, which cannot be generated from MyRIO digital output pins. The digital output pins of MyRIO can generate only a voltage of $3.3V$ and no current. It should be noted that using transistors alone won't activate the target circuit because transistors have large voltage drop from the supplied voltage, V_{CC}, to the collector voltage V_C. For this reason, relays are an essential component of this circuit. The relays act as switches that allow larger voltage to reach the target circuit.

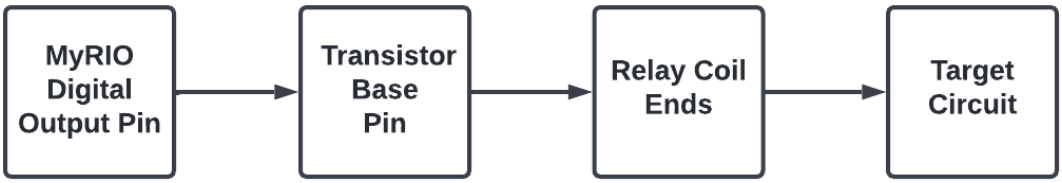

Figure 4.4: Internal trigger circuit sequence.

4.2.2. Transistors

In detail, transistors act as a switch and current amplifiers simultaneously. To activate the transistor, the base-emitter junction should be forward biased. This occurs when the forward base voltage is higher than the emitter voltage, with V_{BE} equal to saturation voltage. To determine value of the base resistor R_B, it is necessary to compute the voltage at the emitter's terminal that is V_E. This voltage can be simply determined because V_{BE} is given in the datasheet and V_B is the voltage of the MyRIO digital output pin.

The gain of the transistor is noted by β. The transistor's current gain is defined as the ratio between the collector current and the base current as shown in Eq.[4.1]. For transistor 2N3094, the gain for a collector current greater than $50mA$ is $\beta = 30$.

$$\beta = \frac{I_C}{I_B} \tag{4.1}$$

Therefore, the section of the base resistance will determine the voltage drop across the base-emitter section and the value of the collector current. However, for this to work, the following conditions should be met:

1. The base transistor should be large enough to create a current that drives the NPN transistor into saturation.
2. The power dissipation of the transistor should be below the value provided in the datasheet.
3. The voltage values should be in the following order $V_E < V_B < V_C <_{VCC}$.

The relay selected needs $5V$ and $65mA$, thus the selected resistor R_B to have a voltage drop of $0.6V$ is determined based on Eq.[4.2].

$$R = \frac{(V_{Do} - 0.6) \times \beta}{0.065} = 1246.15\Omega \tag{4.2}$$

The power across the transistor is $P = V_{CE} \times I_C = 325mW$, which is below the total device power dissipation $650mW$.

In conclusion, by adding NPN transistors as an intermediate step, relays can be activated from MyRIO. The current flowing from the base to the emitter of the transistor controls the relay coil current. An important factor to take into consideration is that the current generated by the transistor should match the power needed to switch the relay, otherwise the target circuit doesn't activate.

4.2.3. Relays

An electro-mechanical relay is used for this circuit. The input section of the relay consists of input terminals that are connected to an electromagnetic coil. When a signal is generated from MyRIO, the transistor switches ON, the current flowing through the relay increases, the electromagnetic coil gets energised and an electrical magnetic flux is generated through the coil. Consequently, the armature is attracted by the magnetic field created by the coil, which moves the contact from the idle position to the working position pin of the relay by acting as a mechanical switch. The armature falls back into the idle position when the transistor switches OFF which makes the current supplied to the relay lower than a threshold value and the coil is de-energized.

The circuit in Figure 4.5 indicates that the base of the transistor is connected to MyRIO digital output, the emitter pin of the transistor is connected to ground and the collector pin of the transistor to the relay's coil.

When the transistor is on, the voltage in the coil increases to match the voltage supplied by the transistor. When the transistor is off, the load in the coil reverses its polarity to keep the current flowing through the coil. This causes the voltage to build up on the coil's connections which are connected to the transistor. In case this voltage builds up, it can damage the NPN transistor. To mitigate this issue a diode is used. As shown in Figure 4.5, the diode is placed with reversed polarity from the power supply and in parallel to the relay's coil. The presence of the diode offers a different path to the current to flow with minimal resistance and can prevent voltage build up.

4.2.4. Circuit Simulation in PSpice

SPICE has built in models for bipolar junction transistors that are helpful to understand the direct current analysis of this circuit and ensure that it is working as desired. First, the circuit is replicated in Spice as shown in Figure 4.5. The relay coils are represented as a 75Ω resistor, obtained by dividing the voltage and current required to activate the relay.

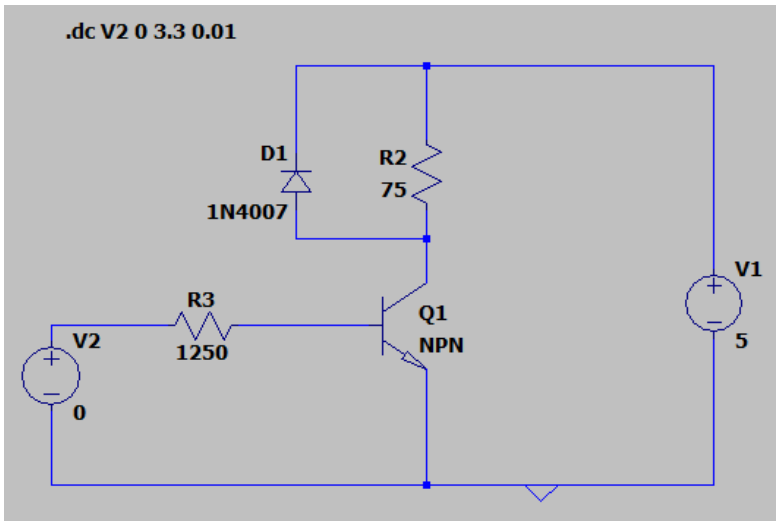

Figure 4.5: Transistor activation circuit in PSpice.

After running the analysis, the obtained data was plotted in Matlab, Figure 4.6. It can be observed that when the base voltage is greater than $0.6V$, the current starts flowing in the collector pin and reaches the $0.065A$, value required to activate the relay.

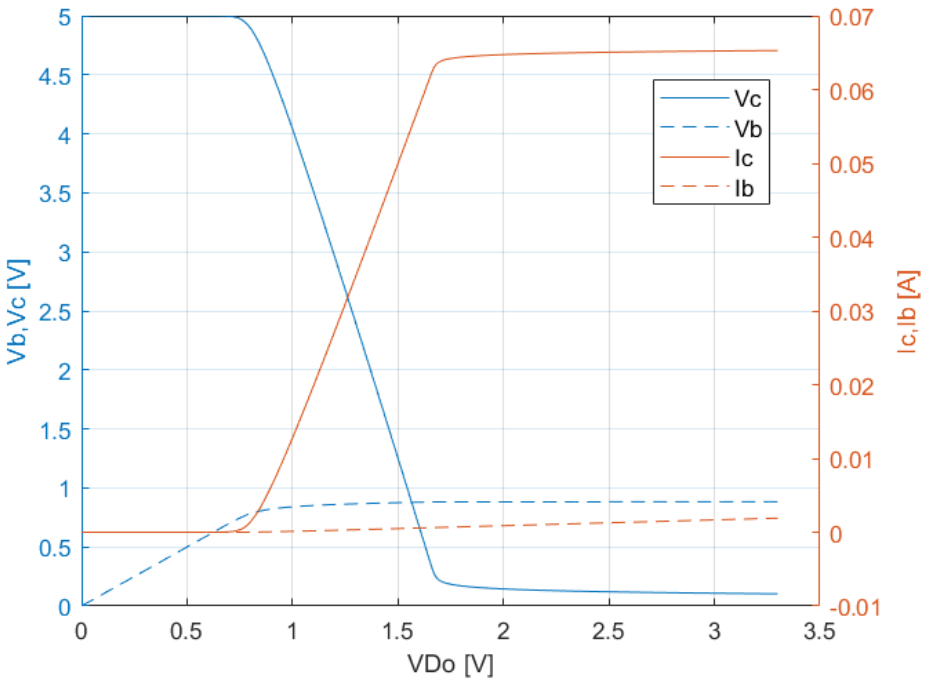

Figure 4.6: Transistor data analysis.

4.3. Heater Controller

The heater power control PCB is designed to generate different output power depending on the desired temperature 4.1 As we are interested in the transient heating phase, the

heater is designed as an open loop controller. The heater control circuit is based on the same concept as the internal trigger circuit. The same sequence will be used: MyRIO, the transistor, the relay, and panel mount resistors. To achieve different power levels for the heater, panel mount resistors are connected to the relay's normally closed pin to ensure voltage drop.

Table 4.1 shows the different temperatures the heater reaches in 10s for specific input powers.

Temperature [°C]	Power [W]
137	42
100	24
73	15
50	10

Table 4.1: Different Temperatures reached by the heater in 10s.

When using a lower voltage, lower power values are obtained which results in a lower heating rate. The heater's resistance is 9.6Ω. To reach the desired powers, panel mount resistors should be added as follows:

1. For $42W$, the supply voltage required for the circuit is $20V$. A resistance of 2Ω and power dissipation of at least $8.4W$ should be added at the output of the relay to drop the voltage from $24V$ to $20V$ with a $2.1A$ current flow.

2. For $24W$, the supply voltage required for the circuit is $15V$. A resistance of 5.69Ω and power dissipation of at least $14.22W$ should be added at the output of the relay to drop the voltage from $24V$ to $15V$ with a $1.58A$ current flow.

3. For $15W$, the supply voltage required for the circuit is $12V$. There is no need for a voltage drop circuit in this case as the supply voltage can be connected to the $12V$ DC/DC regulator.

4. For $10W$, the supply voltage required for the circuit is $10V$. A resistance of 2Ω and power dissipation of at least $2.04W$ should be added at the output of the relay to drop the voltage from $12V$ to $10V$ with a $1.02A$ current flow.

4.4. Thermocouples

T-type and K-type thermocouples are used for the experiment. The data gathered will help us know if the temperature is evenly distributed on the heater surface and if the heat dissipation is producing the density change we are observing with Schlieren photography. The total number of the thermocouples used during the experiment is seven. Inside the blind spot of the heater and near the heater's surface, three type K thermocouples with extension wires are used because they have a temperature range of $[0-250]^{\circ}$C compared to type T thermocouples that can reach a maximum 200°C. Type T thermocouples will be positioned in a symmetric way away from the heater's surface.

The block diagram of thermocouple conditioning to fit the input of the Data Acquisition System (DAS), in this case MyRIO, and eliminate any noise in the temperature measurement is shown in Figure 4.7.

Figure 4.7: Thermocouples conditioning circuit.

4.4.1. Amplification

Thermocouples functionality is based on the Seebeck effect: the greater the difference in temperature, the greater the voltage. This means that the amount of thermo-electric voltage that the thermocouple produces is based on the difference in temperature between the two ends of the sensor. Thus, to measure the temperature one of the junctions is kept at a known reference temperature, usually it is the cold junction is placed in an ice bath. Cold junction compensation is the process of using automatic compensation to get the absolute temperature reading when the cold junction is not at the ice point (0 $^{\circ}C$).

The AD595 IC from Analog Devices is a complete instrumentation amplifier with a cold junction compensator. This amplifier was chosen because it combines ice point reference with a pre-calibrated amplifier to produce a linear output of $10mV/^{\circ}C$ directly from the thermocouple signal. The AD595 is gain trimmed at the factory to match the transfer characteristics of K-type and T-type thermocouples at $+25^{\circ}C$. The resulting gain for AD595 is 247.3, that is obtained by dividing the sensitivity, $10mV/^{\circ}C$, to the Seebeck coefficient, $40.44\mu V/^{\circ}C$ for a type K thermocouple. The device induces an input offset to the output amplifier of $11\mu V$ because the AD595 is trimmed for a $250mV$ output at $+25^{\circ}C$. The functional block diagram of AD595 along with the pin connections are explained in Figure 4.8 from the data sheet [20].

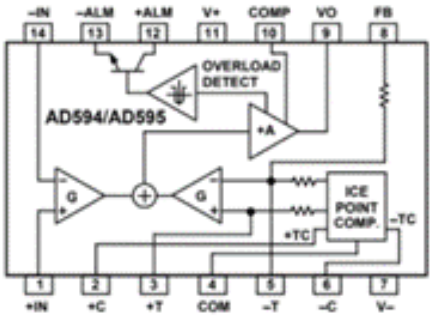

Pin 1	Thermocouple negative end (Constantan)
Pin 14	Thermocouple positive end (Iron)
Pin 4	Ground
Pin 7	Ground
Pin 8	Connected to Pin 9
Pin 9	Output Voltage
Pin 11	+5V

Figure 4.8: AD595 Schematics and connections.

4.4.2. Noise Filtering

An additional operational amplifier is required to act as an active filter to reduce the noise in the measurements. Operational amplifiers are usually used in the construction of active filters, for this experiment LM358 was chosen. The connections of LM358 amplifier are represented in Figure.4.9 from [21].

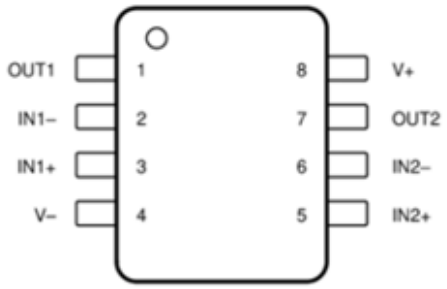

Pin 1	C3
Pin 2	Pin 1
Pin 3	R5; R4; R6; C3; C4
Pin 4	Ground
Pin 5	R1; R2; R3; C1; C2
Pin 6	Pin 7
Pin 7	C1
Pin 8	5V

Figure 4.9: LM358 pins and connections.

Sallen-Key unity gain low-pass filter is implemented. The second order filter is shown in Figure 4.10.

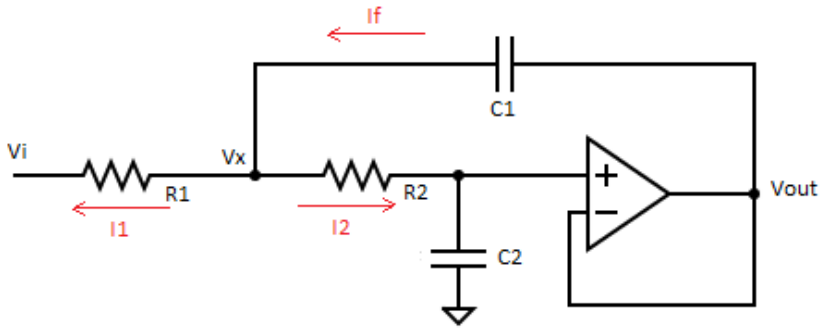

Figure 4.10: Second order filter circuit.

According to Kirchoff's Current Law: $I_f = I_1 + I_2$

According to Ohm's law:

$$I_f = (V_{out} - V_x)sC_1 \tag{4.3}$$

$$I_1 = \frac{V_{out} - V_x}{R_1} \tag{4.4}$$

$$I_2 = V_{out}sC_2 \tag{4.5}$$

The potential divider equation for V_x and V_{out} is applied to determine V_x.

$$V_x = V_{out}(1 + sC_2R_2) \tag{4.6}$$

After substituting Eq.[4.6] into Kirchoff's Current Law, the transfer function of the system is derived, and then the bode plot its obtained, Figure 4.11.

$$\frac{V_{out}}{V_i} = \frac{1}{s^2 + \frac{R_1+R_2}{C_1R_1R_2}s + \frac{1}{R_1R_2C_1C_2}} \tag{4.7}$$

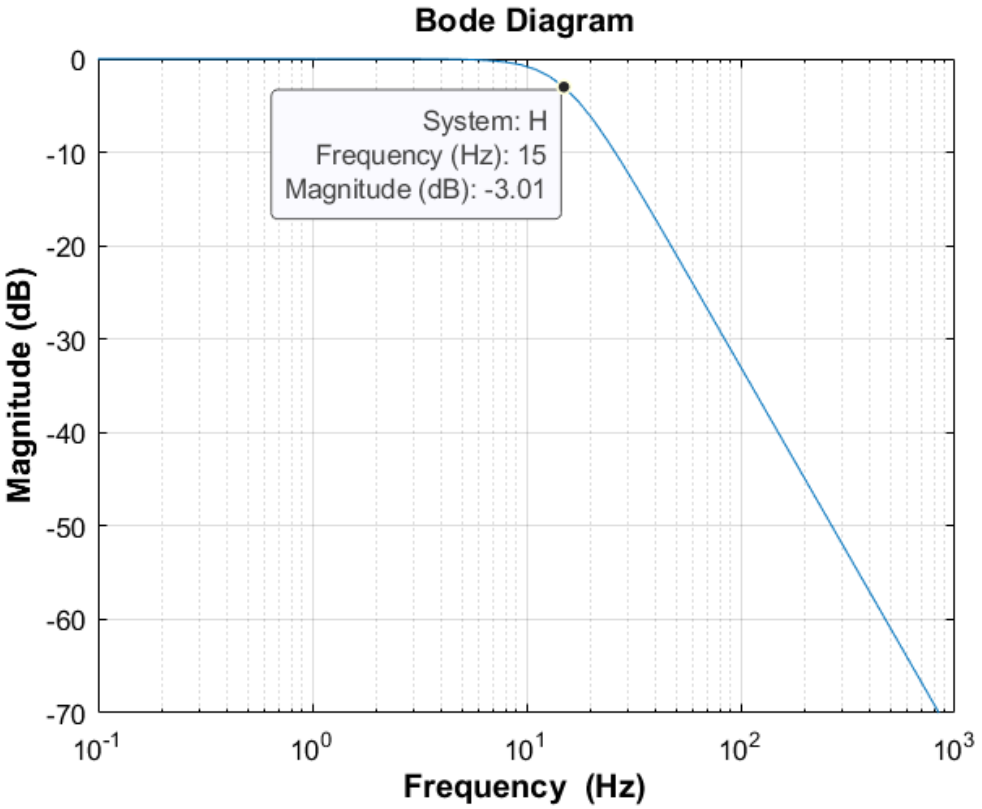

Figure 4.11: Bode plot of low pass filter.

By letting $s = j2\pi f$, the cut-off frequency, f_c, and quality factor, Q, can be written as:

$$f_c = \frac{1}{2\pi\sqrt{R_2R_1C_1C_2}} \tag{4.8}$$

$$Q = \frac{\sqrt{R_1R_2C_1C_2}}{R_1C_1 + R_2C_1} \tag{4.9}$$

The values of the resistors and capacitors were determined based on [22], with $R_1 = mR_2$, $C_2 = nC_2$, and unity gain $K = 1$.

Therefore, from Eq.[4.8] and Eq.[4.9], for a cut-off frequency of $15\ Hz$ and quality factor of 0.707, R_1, R_2, C_1, C_2 can be determined: $R_1 = 20k\Omega$; $R_2 = 12k\Omega$; $C_1 = 1\mu F$; $C_2 = 0.47\mu F$. The cut-off frequency on the bode plot, shown in Figure 4.11, confirms that the values obtained for the resistors and capacitors ensure a cut-off frequency of $15\ Hz$.

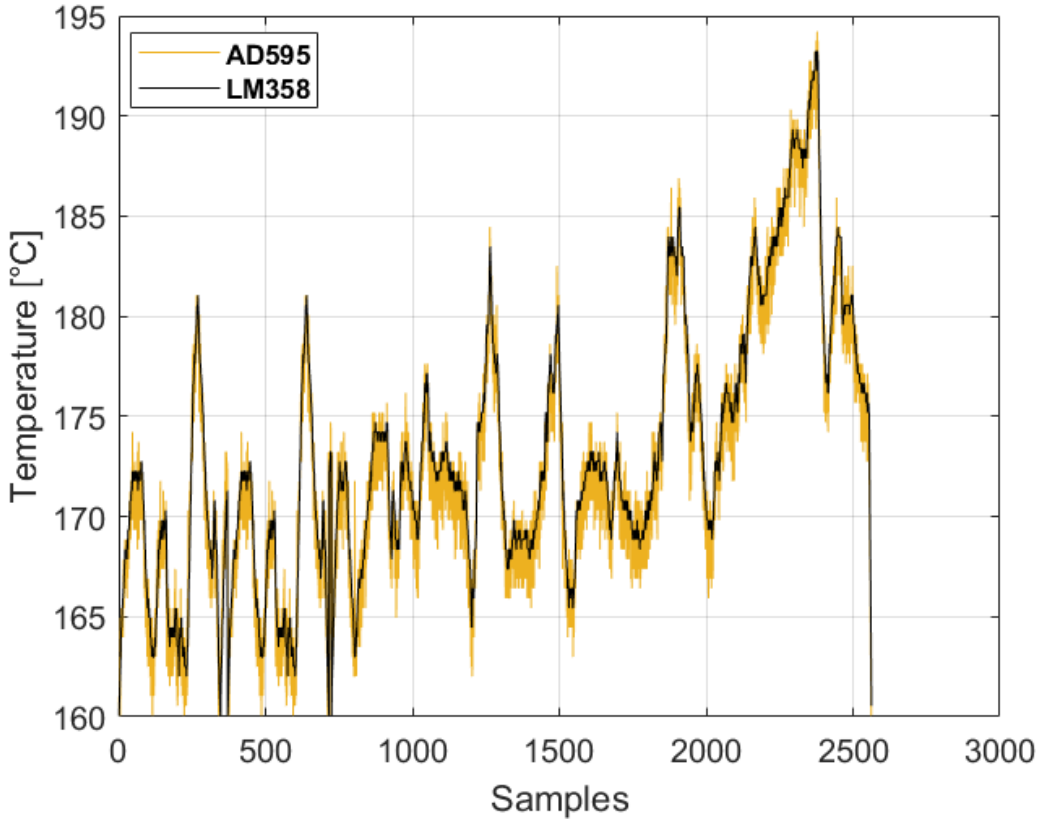

Figure 4.12: Filtered (LM358) and unfiltered (AD595) signal.

To demonstrate the efficiency of the filter, the measurements from the instrumentation amplifier AD595, which is the unfiltered signal, and the measurements at the output of the operational amplifier LM358, the filtered signal, were plotted. It can be observed in Figure 4.12 that the low pass band filter has significantly reduced the noise in the temperature measurements.

4.4.3. Calibration

As thermoucouples output is non-linear, linearization techniques are used to get more accurate readings over a limited temperature range. To calibrate the thermocouple, a already calibrated temperature sensor should be used to compare the measurements.

To perform the calibration in the lab, the multimeter and thermocouples were used simultaneously to gather temperature measurements and compare the readings.

The readings of both sensors were used to compute Eq.[4.10].

$$Y = aX + b \tag{4.10}$$

Where X represents the thermocouple temperature, Y is the reference temperature from the pre-calibrated sensor. From this measurements, variables a and b are extracted and

introduced in the conversion factor used in the temperature acquisition code.

4.5. Led Matrix

4.5.1. Circuit Design

The LED PCB is designed to provide good lighting conditions for the Schlieren imaging. LUXEON 3535L Line LEDs MXA8-PW57-0000 are chosen for the led matrix PCB. The forward maximum voltage for one led is $3.4V$ with $200mA$. The led matrix consists of 7 rows, each row includes a resistor, to ensure a voltage drop from $12V$ to the required circuit voltage, and three LEDs placed in series. As the LEDs are placed in series, the required voltage is at least $V_T = 3 \times 3.4 = 10.2V$. The resistor added should have a value of 10Ω to ensure a voltage drop from $12V$ to $10.2V$, with a current flow of $200mA$ and power dissipation of at least $360mW$.

4.5.2. Thermal Performance

Thermal performance is a critical factor for well-designed LED lighting systems. The main source of heat in a LED comes from the junction between the anode and cathode. This is due to the fact that the LED junction is small, so the energy density is high and the temperature rises rapidly. The led's case temperature was measured with a thermocouple and it reached 70$^{\circ}C$.

4.5.3. Led Matrix test with BOS technique

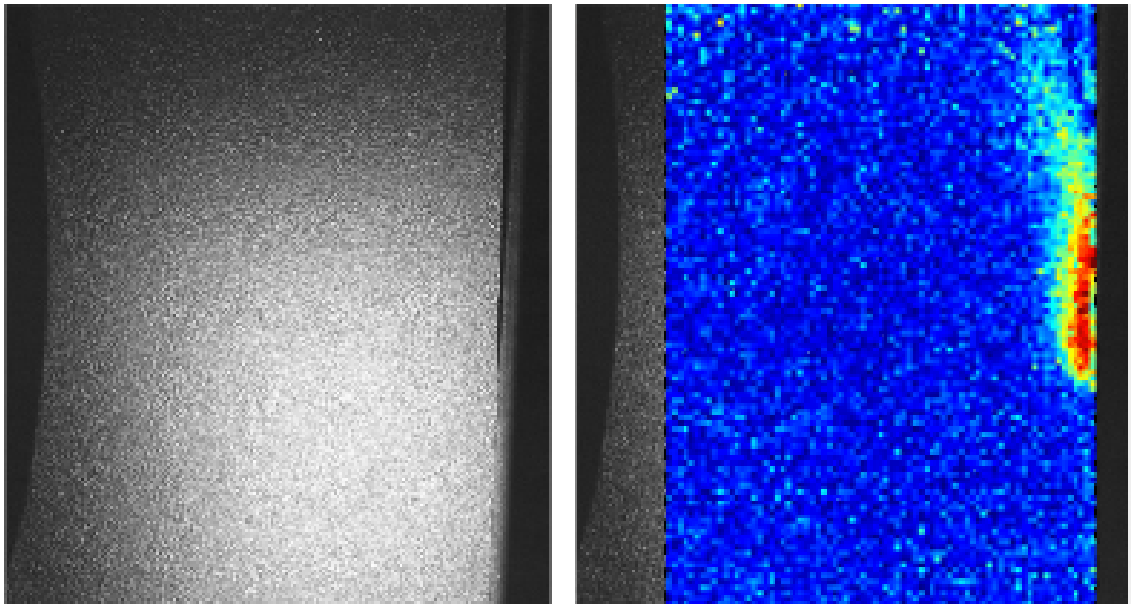

Figure 4.13: Unprocessed and processed image of the heater without acoustics.

The background granulated pattern is illuminated by placing the led matrix behind it, Figure 4.13 (left). As it can be seen in figure 4.13 (right), the led matrix is providing enough illumination to distinguish the pixel shift after processing the video.

CHAPTER 5. PRINTED CIRCUIT BOARDS

5.1. Power Traces

The current capacity of the trace and grounding are two important factors to consider for ease of manufacturing and durability of the PCB.

The width and thickness of conductors on the finished printed board shall be determined according to the current carrying capacity and maximum allowable temperature rise. From Ohm's law, it is known that resistance is inversely proportional to current. For direct current DC, the relation between current, resistance and power is $P = RI^2$. The resistance of a conductor depends on the length, width and resistivity of the material $R = \rho_v L/A$. The resistance of a conductor is expected to be less for a conductor with large cross section area. Hence, traces meant for delivering power signals should be wider due to high current flow requirements. The trace width is computed as follows, first the area of the trace is determined based on Eq.[5.1].

$$A = \frac{I}{k\Delta T^{\beta_1}}^{1/\beta_2} \tag{5.1}$$

Where A indicates the cross-sectional area in [$mils^2$], I the current in [A], and ΔT is the temperature rise above ambient in [°C]. To estimate the coefficients k, β_1, and β_2, it is required to transform them into linear form by using logarithms, as shown in Eq.[5.2].

$$\ln(I) = \ln(k) + \beta_1 \ln(\Delta T) + \beta_2 \ln(A) \tag{5.2}$$

In [23], Eq.[5.2] was analyzed using the cross sectional area from the standard IPC-D-275 for different traces thicknesses, from which the coefficients were obtained Eq:[5.3].

$$\ln(I) = -2.73791 + 0.42827 \ln(\Delta T) + 0.67321 \ln(A) \tag{5.3}$$

Which leads to the current estimation formula Eq.[5.4].

$$I = (0.0647)(\Delta T^{0.428})(A^{0.673}) \tag{5.4}$$

With the cross sectional area A, the width can be determined based on Eq.[5.5]:

$$W = \frac{A}{t \times 1.378} \tag{5.5}$$

Where t is the thickness of the trace [mils] and 1.378 [mils/oz] is associated to the standard thickness for Copper on PCBs for 1 ounce of copper.

The voltage drop across the trace can be determined, but first it is required to find the trace's resistance from Eq.[5.6].

$$R = \rho \frac{L}{tW}(1 + \alpha \Delta T) \tag{5.6}$$

Finally, the voltage drop will be of $V = RI$, that help us know if the voltage drop is very large and if it impacts our design.

5.2. Trigger and Heat controller PCB

The trigger and heat controller PCB were designed on the same plate to reduce the number of connections as these two circuits follow the same sequence of components. The PCB design is presented in Figure 5.4.

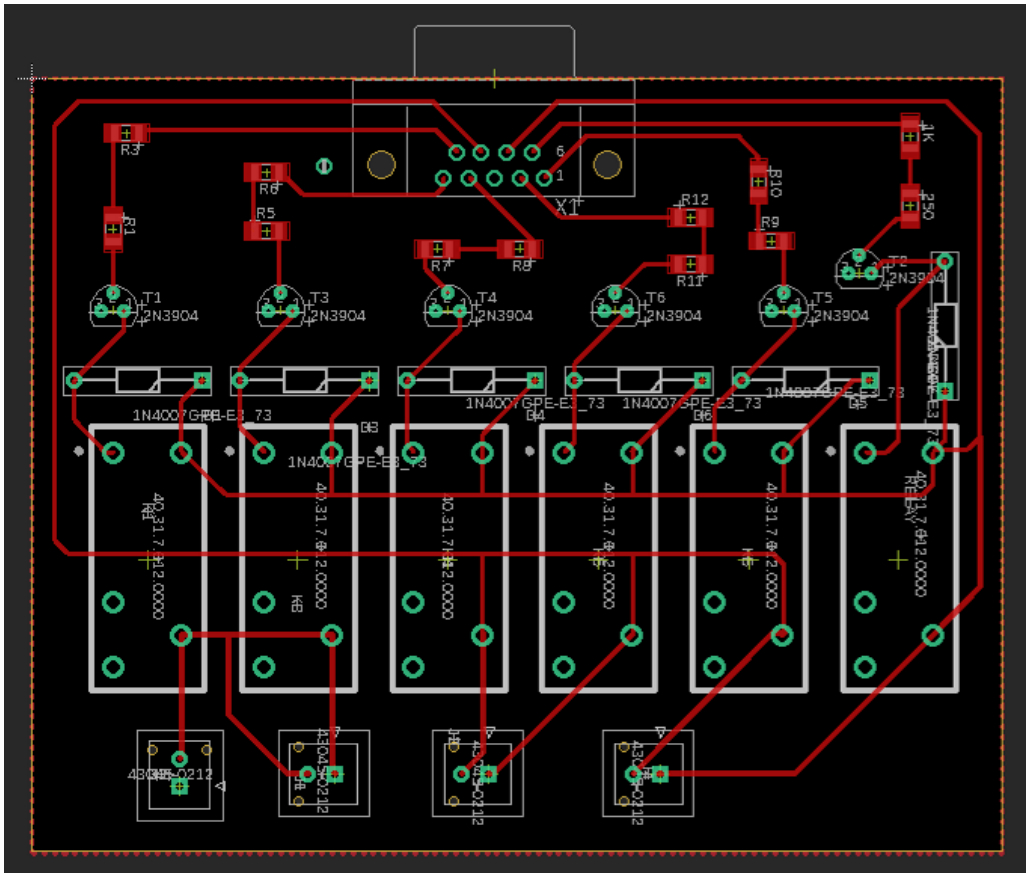

Figure 5.1: Trigger and heat controller PCB schematic in Eagle.

D-sub 9 connector is used to join the cables from MyRio digital output to the PCB. Molex connectors are used to fix the output cables directed to the following circuits.

5.3. Thermocouples PCB

Thermocouple PCB was designed in such a way to keep the noise low and avoid signal distortion. The thermocouples were soldered directly to the AD595CQ amplifiers to obtain more accurate measurements and avoid contact with the copper plate. The interface of this PCB is a D-sub 9 connector with the following connections.

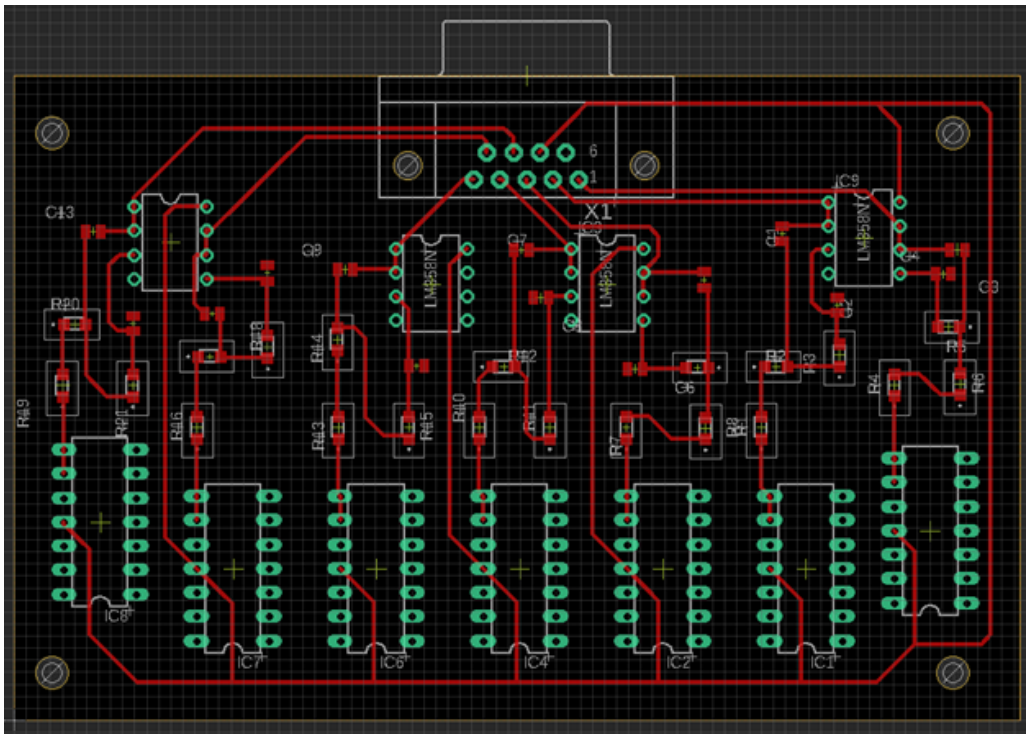

Figure 5.2: Thermocouple PCB design in Eagle.

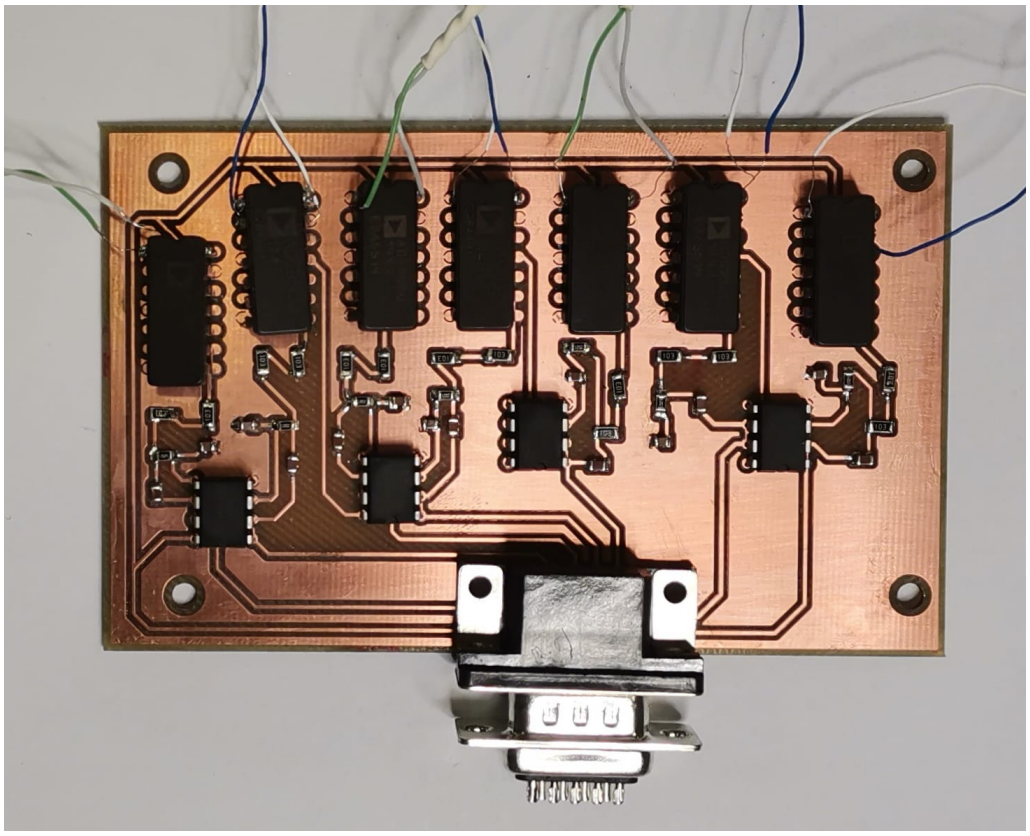

Figure 5.3: Thermocouple PCB soldered.

D-sub 9 pins	Output
1	Thermocouple 1
2	Thermocouple 2
3	Thermocouple 3
4	Thermocouple 4
5	Thermocouple 5
6	Ground
7	Voltage Supply (+5V)

Table 5.1: D-sub 9 connector and output

5.4. LED Matrix PCB

The LED matrix PCB was designed tacking into account the thermal performance of the LEDs and the PCB support. An SMA connector is used to supply voltage to the LED PCB.

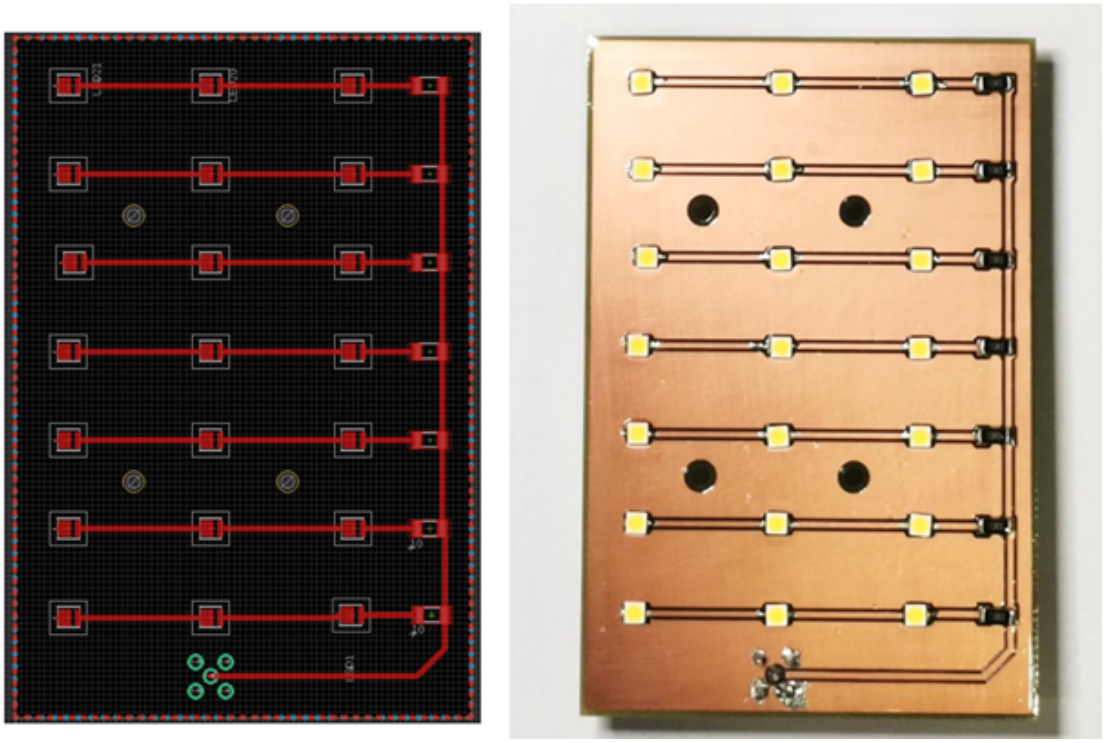

Figure 5.4: Trigger and heat controller PCB schematic in Eagle.

CONCLUSIONS

The aim of this thesis is to design and implement the electronic system of the experiment. This included the definition of the electronics requirements, the choice of different components and devices, design and manufacturing of circuits and PCBs, verification and testing of the design, finally, integration of the electrical part into the capsule and test cell.

The different PCBs mentioned in 5 were designed and tested in the lab. Even though not all the verification process is completed, the circuits tested on bread boards are functioning as expected. For instance: different temperature can be reached by the heater with the heater controller PCB, the illumination for the BOS technique is strong enough, different segments of the experiment can be turned on/off autonomously by the help of the trigger PCB.

The steps left include verification of the PCB according to ECSS-Q-ST-70-08 C standards, calibration of the thermocouples, verification of the noise filtering process and testing the electronics circuits as a whole ensemble. In addition, a check list has to be created in order to determine malfunctions and failures during the lab testings and for the campaign.

For future experiments, a heater controller with feedback loop can be designed. This allows the temperature to be stable and can be helpful to understand the effects of acoustic waves during the stable temperature phase instead of the transient temperature phase. Moreover, the heater can be replaced with a commercial electronic devices that is prone to overheating. This can imply design difficulties as the piezoelectric transducer has to be placed in a strategic position that removes the heat from the surface and avoid the creation of hot spots. In that way the efficacy and efficiency of the acoustic technique can be determined for electric device instead of heater. Schlieren imaging with a parabolic mirror can be used in future experiments to observe the acoustic wave and ensure that a standing wave is produced.

BIBLIOGRAPHY

[1] J.R. Black. Electromigration—a brief survey and some recent results. *IEEE Transactions on Electron Devices*, 16(4):338–347, 1969. doi:10.1109/T-ED.1969.16754. 1

[2] M.Pedram and S. Nazarian. Thermal modeling, analysis, and management in vlsi circuits: Principles and methods. *Proceedings of the IEEE*, 94, 2006. doi:10.1109/JPROC.2006.879797. 1

[3] G. Morrison M. Behnia, L. Maguire. Cooling problems and thermal issues in high power electronics - a multi faceted design approach. *Proceedings of the 5th International Conference on Thermal and Mechanical Simulation and Experiments in Microelectronics and Microsystems, EuroSimE 2004*, pages 519–526, 2004. doi:10.1109/ESIME.2004.1304086. 1

[4] Samuel Tustain. World space observatory-ultraviolet — thermal analysis of spacecraft electronics. https://exchange.esa.int/download/thermal-workshop/workshop2016/parts/WSO-UV.pdf, [Accessed Aug. 22,2022]. 1, 4

[5] José Meseguer, Isabel Pérez-Grande, Angel Sanz-Andrés, and Gustavo Alonso. Thermal systems, 2014. 1

[6] T. Acikalin S.M. Wait V. Suresh Garimella and A. Raman. Experimental investigation of the thermal performance of piezoelectric fans. *Heat Transfer Engineering*, 25:4–14, 2004. doi:10.1080/01457630490248223. 3

[7] Wessel Willems Wits and De Promotiecommissie. Integrated cooling concepts for printed circuit boards, 2008. doi:10.3990/1.9789036527316. 3

[8] B. Farouk. Y. Lin and E. S. Oran. Acoustic wave induced convection and transport in gases under normal and micro-gravity conditions. 2007. doi:10.17918/ETD-1795. 3

[9] S. M. Sohel Murshed and C. A. Nieto de Castro. A critical review of traditional and emerging techniques and fluids for electronics cooling. *Renewable and Sustainable Energy Reviews*, 78:821–833, 2017. doi:10.1016/J.RSER.2017.04.112. 3

[10] Active Thermal Control System (ATCS) Overview - NASA. *NASA*. https://www.nasa.gov/pdf/473486main_iss_atcs_overview.pdf; [Accessed Jul. 7, 2022]. 3

[11] P. I. Cooper, J. C. Sheridan, and G. J. Flood. The effects of sound on forced convection over a flat plate. *International Journal of Heat and Fluid Flow*, 7:61–68, 1986. doi:10.1016/0142-727X(86)90044-5. 4

[12] Sinjae Hyun, Dong Ryul Lee, and Byoung Gook Loh. Investigation of convective heat transfer augmentation using acoustic streaming generated by ultrasonic vibrations. *International Journal of Heat and Mass Transfer*, 48:703–718, 1 2005. doi:10.1016/J.IJHEATMASSTRANSFER.2004.07.048. 4

[13] G. Musielak and D. Mierzwa. Enhancement of convection heat transfer in air using ultrasound. *Applied Sciences 2021, Vol. 11, Page 8846*, 11:8846, 9 2021. doi:10.3390/APP11198846. 4

[14] K. Prodanov. Experimental investigation of the effects of acoustic waves on natural convection heat transfer from a horizontal cylinder in air, 2021. https://digitalcommons.calpoly.edu/cgi/viewcontent.cgi?article=3803context=theses; [Accessed Jul. 16, 2022]. 4

[15] G. Quintana-Buil and R. González-Cinca. Acoustic effects on heat transfer on the ground and in microgravity conditions. *International Journal of Heat and Mass Transfer*, 178:121627, 2021. doi:10.1016/J.IJHEATMASSTRANSFER.2021.121627. 4

[16] Varun Kumar, Mohammed Azharudeen, Charish Pothuri, and Karthick Subramani. Heat transfer mechanism driven by acoustic body force under acoustic fields. *Physical Review Fluids*, 6, 7 2021. 4

[17] https://www.zarm.uni-bremen.de/en/drop-tower/experiment-support.html; [Accessed Jul. 17, 2022]. 7, 8

[18] https://export.rsdelivers.com/es/product/tracopower/tep-150-2415wi/convertidor-dc-dc-150w-salida-24v-dc-63a-04-si-no/6662843 ; [Accessed Jul. 17, 2022]. 10

[19] https://www.tracopower.com/int/es/series/ten-20wir; [Accessed Jul. 17, 2022]. 10

[20] https://docs.rs-online.com/be0a/0900766b814f496a.pdf; [Accessed Jul. 17, 2022]. 15

[21] https://www.ti.com/lit/ds/snosbt3j/snosbt3j.pdf?ts=1658033310459ref; [Accessed Jul. 17, 2022]. 16

[22] Analysis of the sallennkey architecture mixed signal products - Application Report. *Texas Instruments*, 1999. https://www.ti.com/lit/an/sloa024b/sloa024b.pdf; [Accessed Jul. 1, 2022]. 17

[23] D. Brooks. Temperature rise in pcb traces. 1998. Proceedings of the PCB Design Conference West, Miller Freeman, Inc. 21